Available online at www.sciencedirect.com
ScienceDirect
Journal of the European Ceramic Society 29 (2009) 2815–2822
www.elsevier.com/locate/jeurceramsoc

$SrCo_{0.9}Sc_{0.1}O_{3-\delta}$ perovskite hollow fibre membranes for air separation at intermediate temperatures

Bo Meng [a,1], Zhigang Wang [a,1], Xiaoyao Tan [a,*], Shaomin Liu [b,2]

[a] *School of Chemical Engineering, Shandong University of Technology, Zibo 255049, PR China*
[b] *Department of Chemical Engineering, Curtin University of Technology, Perth, WA 6845, Australia*

Received 30 January 2009; received in revised form 23 March 2009; accepted 31 March 2009
Available online 2 May 2009

Abstract

$SrCo_{0.9}Sc_{0.1}O_3$ (SCSc) perovskite powders with sub-micron particle size were synthesized by a modified Pechini method combined with a post-treatment of sintering and ball-milling. From the prepared powders, the SCSc hollow fibre membranes with asymmetric structure and gas-tight property were fabricated by spinning a polymer solution containing 58.4 wt% SCSc followed by sintering at 1200 °C for 5 h. The oxygen permeation properties of the obtained SCSc fibres were measured under air/He gradients at 500–800 °C. This showed the oxygen flux of 1 mL cm^{-2} min^{-1} at 750 °C and 4.41 mL cm^{-2} min^{-1} at 900 °C. Modeling analysis reveals that the oxygen permeation process is predominated by oxygen surface exchange kinetics with an activation energy of 95.0 kJ mol^{-1}. The SCSc membranes showed excellent oxygen permeation performance while exhibiting high structural and permeating stability at intermediate temperatures (500–800 °C).

Keywords: Hollow fibre; Perovskite membrane; Oxygen permeation; Air separation; Intermediate temperature

1. Introduction

Oxygen is an important chemical widely used in many industrial processes and other special fields like military, aerospace and medical applications. In particular, global climate change is challenging the traditional fossil energy technology with high CO_2 emission to atmosphere. The use of pure oxygen instead of air is able to reduce carbon emissions by CO_2 capture. Currently purified oxygen is produced using cryogenic distillation or pressure/vacuum swing adsorption (PSA) technique is too expensive and energy intensive for use in the power industry. One technology gaining significant interest recently is the ceramic membrane process, which is considered to be an economically promising technique with the potential to reduce the oxygen production cost by 30% compared to the conventional methods.[1] The dense ceramic membranes are made from mixed ionic and electronic conductors (MIECs) which separate oxygen at elevated temperatures through the surface exchange reaction and bulk diffusion mechanism as shown in Fig. 1.[2,3] In order to further reduce the energy consumption and assembling cost in practical applications, the operating temperature has to be decreased, which may be achieved either by using novel membrane materials with higher oxygen permeability or by increasing the membrane area per unit volume.

Perovskite oxides with the general structure ABO_3, where elements for the A site can be chosen from calcium, barium, strontium, cerium or other rare earth metals to form 12 coordination with adjacent oxygen ions, and the B site can be occupied by the transition metal ions like cobalt and iron, have been demonstrated to possess excellent oxygen ionic conductivity and oxygen permeability.[4–8] According to the literature, perovskites containing cobalt such as $SrCoO_{3-\delta}$ (SC)-based solid solutions have the highest oxygen permeability.[8–13] However, these perovskites must be structurally stabilized by substituting $SrCoO_{3-\delta}$ oxides with proper cations to form a solid solution.[14–19] Nagai et al.[20] studied the relationship between cation substitution and stability of perovskite structure in SC-based mixed conductors, and found that $SrCo_{0.9}Nb_{0.1}O_{3-\delta}$ exhibits the most stable perovskite structure and the high-

* Corresponding author. Tel.: +86 533 2786292; fax: +86 533 2786292.
E-mail addresses: cestanxy@yahoo.com.cn (X. Tan), Shaomin.Liu@curtin.edu.au (S. Liu).
[1] Tel.: +86 533 2786292; fax: +86 533 2786292.
[2] Tel.: +61 8 92669056; fax: +61 8 92662681.

0955-2219/$ – see front matter © 2009 Elsevier Ltd. All rights reserved.
doi:10.1016/j.jeurceramsoc.2009.03.035

Nomenclature

Notation

D_V	effective diffusivity of oxygen vacancy (cm^2/s)
F	gas feed flow rate (mol/s)
k_r	reverse surface exchange reaction rate constant ($mol/(cm^2\ s)$)
k_f	forward surface exchange reaction rate constant ($cm/(Pa^{0.5}\ s)$)
l	length variable of the hollow fibre membrane (cm)
p_a	atmosphere pressure (1.013×10^5 Pa)
p_l, p_s	pressure in the lumen and the shell side (Pa)
p'_{O_2}, p''_{O_2}	oxygen partial pressure in the air- and the sweep-side (Pa)
P_{O_2}	oxygen permeation flow rate (mol/s)
R	gas constant (8.314 J/(mol K))
R_m	algorithmic radius of the fibre, $R_m = (R_o - R_{in})/\ln(R_o/R_{in})$
R_{in}, R_o	inner and outer radius of hollow fibre (cm)
T	permeation temperature (K)
V_s, V_l	volumetric flow rate of the shell and the lumen gas stream (cm^3/s)
y	oxygen concentration in permeate or sweep-side (%)

est oxygen permeability. Recently, Sc partially substituted $SrCo_{0.95}Sc_{0.05}O_{3-\delta}$ oxide was also found to exhibit both high oxygen permeability and high structural stability but displayed a low mechanical strength.[21]

The ceramic hollow fibre membranes fabricated via the spinning/sintering process have attracted considerable interests in recent years due to the large membrane area per unit volume and ease of high temperature sealing compared to the conventional disc and tubular forms.[22–27] These hollow fibre membranes usually possess an asymmetric structure consisting of a dense layer and porous substrate, which are formed in the spinning process, and exhibit noticeably less resistance to oxygen permeation. However, the hollow fibres must possess high mechanical strength to be assembled into modules for the commercial applications.

In this study, we reported the development of $SrCo_{0.9}Sc_{0.1}O_{3-\delta}$ (SCSc) perovskite hollow fibre membranes with both good mechanical strength and favorable oxygen fluxes at intermediate temperatures (500–800 °C). The oxygen permeation properties of the prepared SCSc membranes were investigated both experimentally and theoretically.

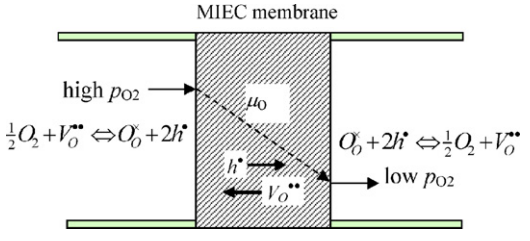

Fig. 1. Schematic of oxygen permeation across mixed ion-electron conducting membranes.

2. Experimental

2.1. Materials

$Sr(NO_3)_2$ (>99.9%), $Co(NO_3)_2{\cdot}6H_2O$ (>99.9%, both from Kermel Chem Inc., Tianjin, China), and $Sc(NO_3)_3$ (>99.99%, Yutai Fine Chemicals Ltd., Shandong) were used as metallic precursors for the preparation of $SrCo_{0.9}Sc_{0.1}O_{3-\delta}$ (SCSc) powders. Citric acid (>99%, Ajax) and ethylene diamine tetraacetic acid (EDTA) (AR, Longjili, Tianjin) were used as complexing agents. Nitric acid and ammonium hydroxide were used to adjust the pH of starting solution. Polyethersulfone, (PESf) [(Radel A-300), Ameco Performance, USA] and N-methyl-2-pyrrolidone (NMP) [AR Grade, purity >99.8%, Kermel Chem Inc., Tianjin, China] were used to prepare the spinning suspension. Polyvinylpyrrolidone (PVP, K90) [GAF® ISP Technologies, Inc. Mw = 630,000] was used as an additive. Deionized water and tap water were used as the internal and external coagulants, respectively.

2.2. Preparation of $SrCo_{0.9}Sc_{0.1}O_{3-\delta}$ powders

$SrCo_{0.9}Sc_{0.1}O_{3-\delta}$ (SCSc) oxide powders were synthesized by a modified Pechini technique. EDTA powder was dissolved in aqueous ammonium hydroxide (28.0–30.0%). Stoichiometric quantities of $Sr(NO_3)_2$, $Co(NO_3)_2$ and $Sc(NO_3)_3$ together with some amount of citric acid in granular form were then added in the above EDTA solution under constant stirring. To avoid precipitation, a pH of 3–4 was maintained in the mixture using nitric acid and ammonium hydroxide. Molar ratios of EDTA, citric acid, and total metal ions in the final solution were 1:2:1. The transparent solution was heated at 80 °C for 4–5 h under continuous stirring to remove the excess water until a viscous gel was formed. The gel was heated by a hot plate. As the temperature was increased to around 450 °C, auto-combustion took place to form a fluffy black powder, i.e., the SCSc powder precursor. Under an air flow, the powder precursor was calcined at 800–1000 °C for 5 h in a furnace to remove the residual carbon and form the desired structure. For spinning hollow fibre membranes, the powders calcined at 900 °C were ball-milled for 48 h, followed by sieving to a 200-mesh to exclude agglomerates.

2.3. Preparation of $SrCo_{0.9}Sc_{0.1}O_{3-\delta}$ hollow fibre membranes

A dry–wet spinning method was used to fabricate SCSc hollow fibre precursors as described elsewhere.[23] In this work, the spinning solution is composed of 58.4 wt% SCSc powders, 7.5 wt% polyethersulfone (PESf), 33.3 wt% 1-methyl-2-pyrrolidinone (NMP) and 0.8 wt% polyvinyl pyrrolidone (PVP, K90). The hollow fibre precursors were sintered at 1000–1200 °C for 5 h with a continuous air flow of 50 mL min^{-1} to form gas-tight membranes. The preparation conditions are summarized in Table 1.

Table 1
Preparation conditions of the SCSc hollow fibre membranes.

Experimental parameters	Values
Compositions of the starting solution	
$SrCo_{0.9}Sc_{0.1}O_{3-\delta}$	58.4 wt%
PESf, Radel A-300	7.5 wt%
NMP	33.3 wt%
PVP K90	0.8 wt%
Spinning temperature	28 °C
Injection rate of internal coagulant	10.3 mL min^{-1}
Spinning pressure	0.12 MPa
Air gap	1.0 cm
Sintering temperature	1000–1200 °C
Sintering time	5 h
Air flow rate in sintering	50 mL min^{-1}

2.4. Oxygen permeation measurements

Oxygen permeation properties of the SCSc hollow fibre membranes were investigated in an oxygen permeation cell schematically shown in Fig. 2. The SCSc hollow fibre membrane of about 30 cm length was housed in a quartz tube (Φ18 mm diameter and 400 mm length) with 1592 high-temperature silicone sealant (purchased from Tonsan New Materials and Technol. Co., Beijing) that is able to withstand up to 350 °C. The permeation cell was positioned in a Φ22 mm × 180 mm tubular furnace having 50 mm effective heating length. Air was fed to the shell side while helium sweep gas was passed through the fibre lumen to collect the oxygen permeate. The gas feed flow rates were controlled by mass flow controllers (D08-8B/ZM, Shanxi Chuangwei Instrument Co. LTD, China) calibrated using a soap bubble flow meter. Effluent flow rates were measured by the bubble flow meter. Composition of the permeate gas was measured online using a gas chromatograph (Agilent 6890N) fitted with a 5 Å molecular sieve column (Φ3 mm × 3 m) and a TCD detector. Highly pure hydrogen was used as the carrier gas and the flow rate was fixed at 40 mL min^{-1}. GC calibration was performed using a gas standard mixture consisting of 5% oxygen, 5% nitrogen and 90% helium (mole fractions within ±2% accuracy) purchased from Baiyan Gases Ltd. Co., Zibo. All gas composition measurements were made after 20 min following a temperature change or sweep gas rate change. The oxygen permeation rate of the membrane was calculated from the concentration change of oxygen in the helium stream:

$$P_{O_2} = \frac{F_{He} y_{O_2}}{1 - y_{O_2}} \quad (1)$$

where F_{He} is the helium feed flow rate and y_{O_2} is the oxygen concentration in the helium effluent.

2.5. Characterization methods

Thermogravimetric analysis (TGA) and differential thermal analysis (DTA) were conducted in a TG/DTA system (MDSC Q100, TA) with a scanning rate of 10 °C min^{-1}. Ten milligram powder was placed in the sample holder and then heated from room temperature to 1200 °C in air with a flow rate of 50 mL min^{-1}. Weight and the heat flux changes were recorded as a function of temperature.

The crystal phases of the prepared SCSc powders and the hollow fibres were ascertained by X-ray diffraction (BRUKER D8 Advance, Germany) using Cu-Kα radiation (λ = 0.15404 nm). The hollow fibres were ground into fine powders prior to the XRD measurements. Continuous scan mode was used to collect 2θ data from 20° to 80° with a 0.02° sampling pitch and a 2° min^{-1} scan rate. The X-ray tube voltage and current were set at 40 kV and 30 mA, respectively.

Microstructure and morphology of the SCSc powders and the hollow fibres were observed by scanning electron microscopy (SEM) (FEI Sirion-200, the Netherlands). Gold sputter coating was performed on the fibre samples under vacuum before the measurements.

The gas-tightness of the sintered SCSc hollow fibre membranes was tested through a gas permeation measurement as described elsewhere.[28] The hollow fibre was glued to a stainless steel sample holder using epoxy resin. The sample holder was then housed into a stainless steel cylinder in which the pressure was controlled with nitrogen gas. The gas permeance of the hollow fibre membrane could be calculated based on the pressure changes in the cylinder with time.

3. Results and discussion

3.1. SCSc powders

A modified Pechini technique was used to synthesize the SCSc powders where ethylenediaminetetraacetic acid (EDTA) and citric acid (CA) are used as chelating agents to form the complexing solution. Deep-purple transparent gel-like precursor was obtained when the aqueous solution was continuously thickening. Because no precipitation occurred over the entire condensation process, the compositional homogeneity of metal ion distribution on atomic level in the aqueous solution could be well maintained in the resulting gel. Continuous heating of the gel triggered the auto-combustion, during which most of the organics were removed with further heat treatment converting the powders into perovskite structure. Fig. 3 shows the TGA and DTA curves of the SCSc powder precursor after combustion.

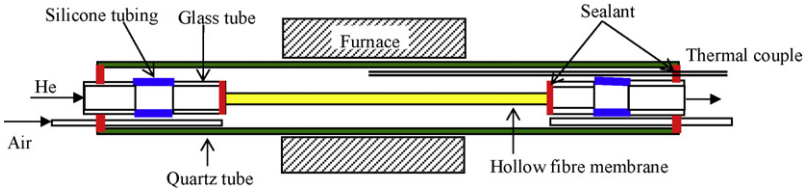

Fig. 2. Schematic graph of the hollow fibre permeation cell.

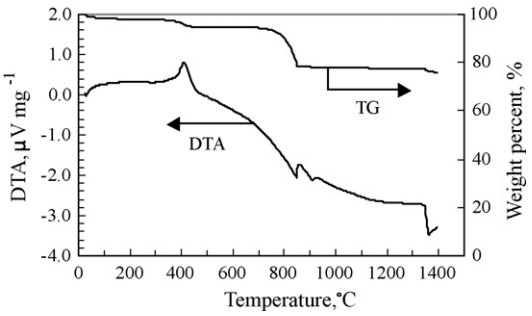

Fig. 3. TGA/DTA curves of the SCSc powders after combustion.

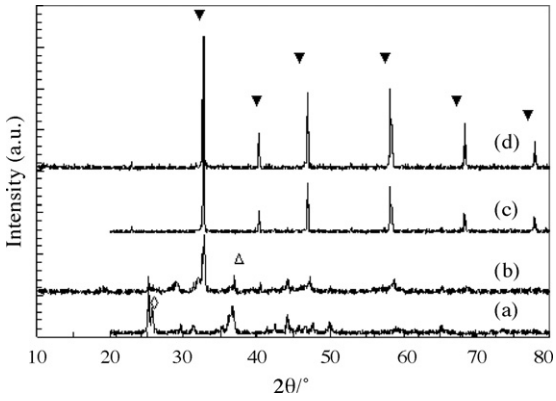

Fig. 4. XRD patterns of the SCSc powders (a) after auto-combustion and (b) sintered at 800 °C, (c) 900 °C and (d) 1000 °C for 5 h (▼, △, ◊ represent the peaks of perovskite, Co_3O_4 and $SrCO_3$, respectively).

As can be seen, the TGA curve shows a two-stage weight loss profile. The first stage with a span of 350–450 °C is attributed to the burnout of carbon residue left from the previous auto-combustion process, corresponding to a high exothermic peak at around 400 °C on the DTA curve. The second stage is a faster weight loss of about 15% in the range of 700–860 °C, corresponding to a DTA endothermic peak at around 850 °C. This is due to the thermal decomposition of carbonates to oxides during the formation of perovskite phase. After 900 °C, no more weight loss is noticed as the sample achieves the final perovskite structure.

The crystalline phase development as a function of sintering temperature is depicted by the XRD patterns plotted in Fig. 4. As can be seen, the starting precursor obtained after auto-combustion is a mixture of metal oxides or carbonates such as $SrCO_3$ and Co_3O_4 in addition to other unknown intermediate phases (Fig. 4a). For the samples calcined at 800 °C, the XRD pattern displays the existence of perovskite and SrO phases as shown in Fig. 4b. With sintering temperature above 850 °C, the samples have already reached the pure cubic perovskite phase, which is seen by the characteristic diffraction peaks with the respective 2θ angles at 32.76, 40.3, 46.86, 58.32, 68.46 and 77.96 as shown in Figs. 4c and d. These results further confirm that the formation of perovskite phase starts at around 850 °C.

Fig. 5 displays the morphology of the SCSc perovskite powders for spinning hollow fibres. It can be seen from Fig. 5a that the SCSc particles have shown some agglomeration during the calcination process. These agglomerates can be harmful to the uniform dispersion of SCSc particles in the spinning solution, which brings about defects in the resultant hollow fibres. In order to obtain uniform powders, the post-treatment including ball-milling and sieving were carried out. As can be seen from Fig. 5b, the post-treated powders are very uniform with an average particle size of 0.5 μm. Such a post-treatment is essential to obtain the necessary quality perovskite powders to synthesize gas-tight hollow fibre membranes.

3.2. SCSc hollow fibre membranes

SEM micrographs of the SCSc hollow fibre precursors and sintered fibres are shown in Fig. 6. Fig. 6(1a) shows that the typical outer and inner diameter (o.d./i.d.) of the fibre precursors are around 2.35/1.73 mm, respectively. From Fig. 6(1b), it can be seen that short finger-like structures are present at the outer and inner sides while a sponge-like structure is possessed in the central region of the precursor. The formation of such asymmetric structure can be attributed to the nature of the precipitation as the rapid precipitation occurred at both the inner and outer walls close to coagulants resulting in short finger pores but the slow precipitation at the center of the fibre giving the sponge-like structure.[23] Micrographs of Fig. 6(1c and d) display the inner/outer surfaces of the hollow fibre precursor, from which it can be seen that small SCSc particles are well dispersed and connected with each other by the polymer binder. Fig. 6(2a–d)

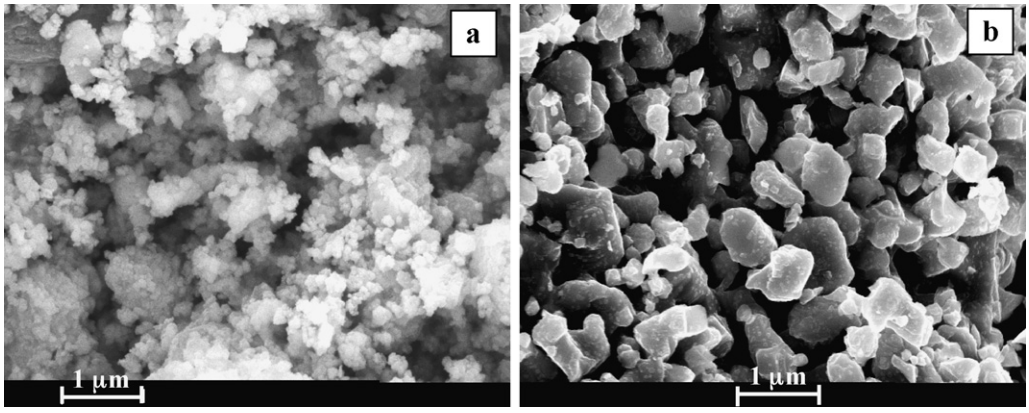

Fig. 5. SEM micrograph of the SCSc powders (a) before milling and sieving, (b) after ball-milling and sieving.

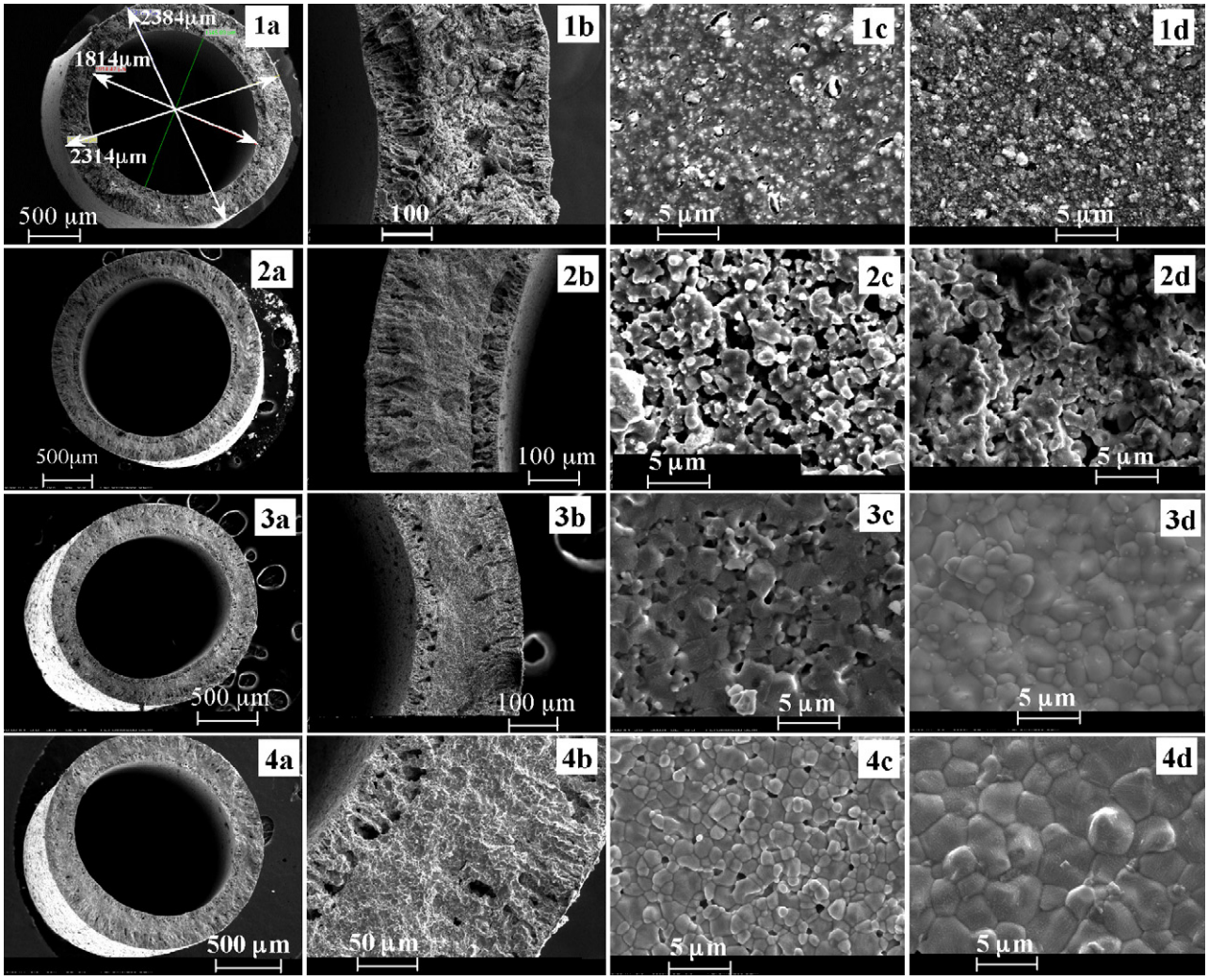

Fig. 6. SEM pictures of (1) the SCSc hollow fibre membrane precursor and the sintered membrane at (2) 1000 °C, (3) 1100 °C, (4) 1200 °C. (a) Cross-section, (b) fibre wall, (c) inner surface, (d) outer surface.

shows the micrographs of the hollow fibres sintered at 1000 °C for 5 h. After sintering, the o.d./i.d. of the fibres shrank from 2.35/1.73 mm to 2.17/1.60 mm, respectively, due to the removal of organics and densification of the porous structure. The cross-sectional structure of the sintered fibres shown in Fig. 6(2b) is similar to that of the fibre precursor suggesting that the sintering does not change the general structure of the hollow fibres. With sintering, the fibres become porous due to the removal of organic binders however the SCSc particles became partly coalesced as shown in Fig. 6(2c and d). When the sintering temperature is increased to 1100 °C, the o.d./i.d. of the fibres further shrank to 1.87/1.34 mm, respectively (Fig. 6(3a)). Fig. 6(3b) shows that although the sandwiched structure is retained, the quantity and size of the pores have greatly reduced after sintering. Furthermore, the SCSc particles grew leading to bigger and clearer grain boundaries as shown in Fig. 6(3c and d). During the gas permeation tests, the hollow fibres sintered at 1100 °C exhibited nitrogen permeability of $\sim 8.7 \times 10^{-4}$ mL cm^{-2} min^{-1} kPa^{-1}, and thus were not completely gas-tight. Accordingly, the sintering temperature was further increased to 1200 °C. Fig. 6(4a–d) displays the microstructure of the resultant hollow fibres. As can be seen, the o.d./i.d. of the fibres became 1.72/1.24 mm, respectively, and the SCSc grain size in the membrane increased to 3–5 μm. The nitrogen permeability of these membranes was less than 1×10^{-6} mL cm^{-2} min^{-1} kPa^{-1}, which was measured by pressure change but could not be detected by bubble flow meters. Therefore, the SCSc hollow fibres have to be sintered at 1200 °C in order to obtain completely gas-tight membranes. The pores on the inner surface (Fig. 6(4c)) have no effect on the gas-tight quality of the membrane as both the central layer and the outside layer provide the necessary densification.

3.3. Oxygen permeation through the SCSc membranes

Oxygen permeation through the SCSc hollow fibre membranes was tested using air as feed in the shell side and helium as sweep gas in the lumen side. At elevated temperatures, oxygen permeates from the air- to the sweep-side in the form of oxide ions under the oxygen concentration gradient across the membrane, resulting in the changes of oxygen concentrations on both the air- and the sweep-side along the hollow fibre. In addition, the permeation temperature also varies with the fibre

length from the inlet because a temperature profile is always present in the furnace tube. In order to analyze the membrane's permeation property, a mathematical model of the permeation cell is presented as follows.

The following assumptions were adopted for the development of the mathematical model: (1) isothermal operation. It implies the permeation of the fibre beyond the constant temperature zone (5 cm) may be neglected as the permeability of the MIEC membranes decreases exponentially with decreasing temperature; (2) plug flow for both the air and the sweep gas; (3) independence of the surface exchange rate constants and vacancy diffusion coefficient with oxygen partial pressure; (4) negligible mass transfer resistance between the gas and the membrane surface; (5) ideal gas behavior. The mass conservation equations for the shell and lumen gas streams can be written, respectively, as:

$$\text{Shell side for oxygen}: \frac{d}{dl}\left(\frac{p'_{O_2}V_s}{RT}\right) = -2\pi R_m J_{O_2} \quad (2)$$

$$\text{Shell side for nitrogen}: \frac{(p_s - p'O_2)V_s}{RT} = 0.79F_{Air} \quad (3)$$

$$\text{Lumen side for oxygen}: \frac{d}{dl}\left(\frac{p''_{O_2}V_l}{RT}\right) = 2\pi R_m J_{O_2} \quad (4)$$

$$\text{Lumen side for helium}: \frac{(p_l - p''_{O_2})V_l}{RT} = F_{He} \quad (5)$$

with the boundary condition:

$$l = 0, \quad p'_{O_2} = 0.21p_a, \quad p''_{O_2} = 0 \quad (6)$$

where p'_{O_2} and p''_{O_2} are the oxygen partial pressures in the air- and the sweep-side, respectively; V_l and V_s are the volumetric flow rates of the lumen and the shell gas stream; p_l and p_s are respectively the pressures in the lumen and shell side, and here equal to atmospheric pressure, i.e., $p_l = p_s = p_a = 1.013 \times 10^5$ Pa; R_m the logarithmic radius, $R_m = (R_o - R_m)/\ln(R_o/R_{in})$, in which R_o and R_{in} are respectively the outer and the inner radius of the fibre; F_{Air} and F_{He} are the molar feed flow rate of air and sweep gas, respectively; R is ideal gas constant and T is the operating temperature. The local oxygen permeation flux through the MIEC hollow fibre membranes, J_{O_2} can be given by[28–30]:

$$J_{O_2} = \frac{k_r\left[(p'_{O_2})^{0.5} - (p''_{O_2})^{0.5}\right]}{R_m/R_o(p''_{O_2})^{0.5} + (2k_f(R_o - R_{in})/D_V)(p'_{O_2}p''_{O_2})^{0.5} + R_m/R_{in}(p'_{O_2})^{0.5}} \quad (7)$$

where D_V is the diffusion coefficient of oxygen vacancy; and k_f and k_r are, respectively, the forward and the reverse reaction rate constants for the surface exchange reaction:

$$\frac{1}{2}O_2 + V_o^{\bullet\bullet} \overset{k_f/k_r}{\longleftrightarrow} O_o^x + 2h^{\bullet} \quad (8)$$

where the charged defects are defined using the Kröger–Vink notation. That is, $O_o^{\times}$ stands for lattice oxygen, $V_o^{\bullet\bullet}$ for oxygen vacancy and $h_i^{\bullet}$ for electron hole.

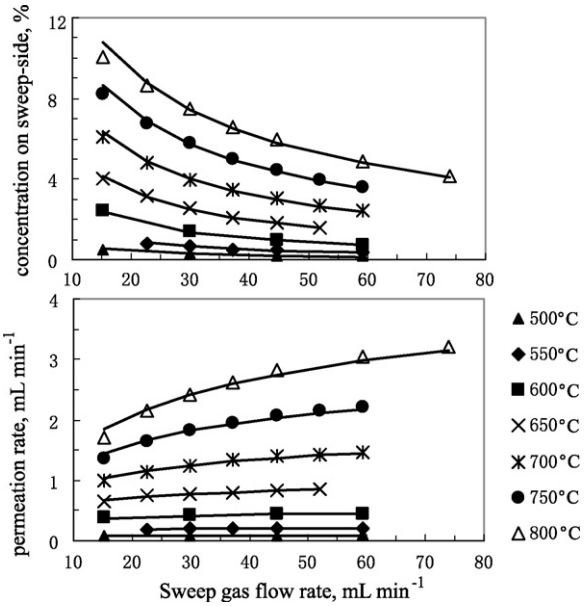

Fig. 7. Effect of sweep gas flow rate on (a) the oxygen permeate concentration and (b) the oxygen permeation flux through the SCSc hollow fibre membranes at different temperatures (effective membrane area = 2.06 cm^2).

For the membranes having a small thickness, the permeation at lower temperatures is mainly controlled by the surface exchange kinetics.[21,30] Eq. (7) then reduces to:

$$J_{O_2} = \frac{k_r\left[(p'_{O_2})^{0.5} - (p''_{O_2})^{0.5}\right]}{R_m/R_o(p''_{O_2})^{0.5} + R_m/R_{in}(p'_{O_2})^{0.5}} \quad (9)$$

Fig. 7 shows the oxygen permeate concentration and the overall oxygen permeation rate as a function of helium sweep gas flow rate at intermediate temperatures (500–800 °C), where the air feed flow rate is fixed at 200 mL min^{-1}. As expected by increasing sweep flow rate at a given permeation temperature, the oxygen concentration decreases in the sweep-side and hence the driving force for oxygen permeation is increased. This improvement leads to an increased oxygen permeation rate, as shown in Fig. 7b. However, such an increase in oxygen permeation rate is minimal at lower temperatures as the permeation rate is more limited by temperature activation than by driving force. On the other hand, for a fixed sweep gas flow rate, the oxygen permeation rate increases with increasing temperature as both the exchange reaction rate and the ionic diffusion rate show temperature activation. This leads to an increase in the oxygen permeate concentration implying that the operating temperature plays a more important role than the driving force in oxygen permeation through SCSc membranes. The modeling results based on Eq. (9) are also plotted with the solid curves in Fig. 7, where the surface exchange reaction constants are obtained by regressing the experimental data with the least squares method. It can be seen that the experimental data are in excellent agreement with the modeling results. Moreover, the relationship between the surface exchange reaction constant, k_r and temperature can be depicted quite well with Arrhenius equation ($R^2 = 0.998$), as shown in Fig. 8. Such results indicate the oxygen permeation process in the SCSc hollow fibre membranes

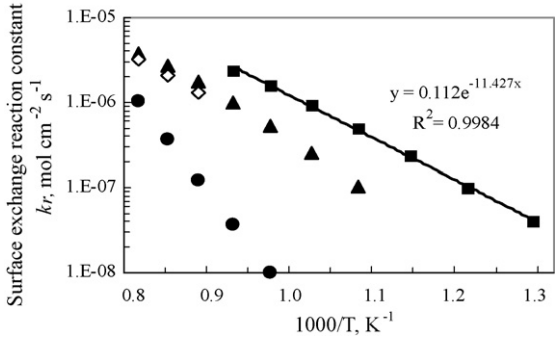

Fig. 8. Plot of the surface exchange reaction constant against temperature (■ this work; ● $La_{0.6}Sr_{0.4}Co_{0.2}Fe_{0.8}O_{3-\delta}$ (LSCF) disc membrane[3]; ◊ $Ba_{0.5}Sr_{0.5}Co_{0.8}Fe_{0.2}O_{3-\delta}$ (BSCF) fibre membrane[30]; ▲ highly asymmetric LSCF fibre membrane[31]).

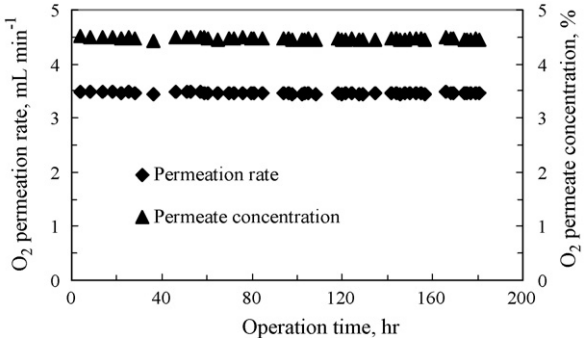

Fig. 10. Long-term test of oxygen permeation (operating temperature = 800 °C, air feed flow rate = 180 mL min^{-1}, sweep gas flow rate = 74 mL min^{-1}, effective membrane area = 2.06 cm^2).

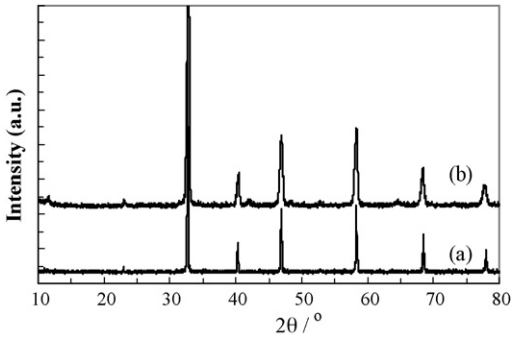

Fig. 11. XRD patterns of (a) the fresh hollow fibre membrane and (b) the used SCSc fibre after oxygen permeation measurements.

is controlled by the surface exchange kinetics in the temperature range of 500–800 °C. The activation energy obtained from the slope of the Arrhenius line is $E_a = 95.0\,kJ\,mol^{-1}$, which is close to that for the $SrSc_{0.05}Co_{0.95}O_{3-\delta}$ disc membranes.[21] For a better comparison, the surface exchange reaction constants of the $Ba_{0.5}Sr_{0.5}Co_{0.8}Fe_{0.2}O_{3-\delta}$ (BSCF)[30] and $La_{0.6}Sr_{0.4}Co_{0.2}Fe_{0.8}O_{3-\delta}$ (LSCF)[3,31] membranes are also plotted in Fig. 8. From this comparison, it can be seen that the k_r for the SCSc membrane may be of at least one order of magnitude higher than that for the LSCF and BSCF membranes in the lower temperature range. This means the SCSc hollow fibre membranes possess much better low-temperature permeation performance than the other membranes. For example, the SCSc membrane could provide 1 mL cm^{-2} min^{-1} (calculated by 5 cm fibre length with 2.06 cm^2 membrane area) permeation flux at temperature as low as 750 °C, whereas LSCF or BSCF membranes required temperatures higher than 850 °C to provide the same permeation rate.

Fig. 9 compares the experimental permeation rates with the modeling results at different temperatures, where the sweep and the air feed flow rates are fixed at 59.3 and 200 mL min^{-1}, respectively. It can be seen that the experimental data agrees well with the modeling results although the permeation rate constant k_r was obtained only from the low-temperature data. As the temperature is increased from 500 to 900 °C, the overall oxygen permeation rate increases from 0.09 to 6.25 mL min^{-1}. However, if the sweep gas flow rate is increased to 147 mL min^{-1}, the oxygen permeation rate can attain up to 9.53 mL min^{-1} at 900 °C with the corresponding permeate concentration of 7.16%. That is to say, the oxygen permeation flux through the SCSc hollow fibre membranes may reach at least 4.41 mL cm^{-2} min^{-1} at 900 °C, which is much higher than those obtained from other MIEC membranes.

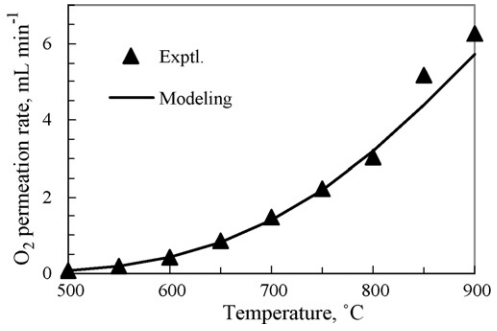

Fig. 9. Effect of temperature on the oxygen permeation through the SCSc membrane (He flow rate = 59.2 cm^3 min^{-1}; air feed flow rate = 200 cm^3 min^{-1}, effective membrane area = 2.06 cm^2).

A long-term operation test was also conducted on the SCSc hollow membranes under the condition of 800 °C, 74 mL min^{-1} sweep gas and 180 mL min^{-1} air feed flow rates. The oxygen permeate concentration and the permeation rate plotted against operation time are shown in Fig. 10. As can be seen, the oxygen permeation rate varies within a very narrow range, i.e., from 3.45 to 3.50 mL min^{-1} in the entire 181 h duration. This shows that the SCSc membrane is very stable when operated at intermediate temperatures. Its stability has been also further confirmed by the XRD measurements on the used and the fresh fibre membranes. The perovskite structure has been well preserved after the long-term permeation test, as shown in Fig. 11.

4. Conclusions

$SrCo_{0.9}Sc_{0.1}O_3$ (SCSc) powders having a sub-micro particle size were synthesized by a modified Pechini method. In order to make the powders appropriate for spinning hollow fibre membranes, the post-treatment including sintering at 900 °C and ball-milling is necessary. Gas-tight SCSc hollow

fibre membranes with an asymmetric structure can be fabricated by spinning a polymer solution containing SCSc powders followed by sintering at 1200 °C for 5 h. The resulted SCSc membranes not only possess high oxygen permeation fluxes, i.e., 1 mL cm^{-2} min^{-1} at 750 °C and 4.41 mL cm^{-2} min^{-1} at 900 °C, respectively, but also exhibit high structural and stable permeating stability at intermediate temperatures (500–800 °C). The oxygen permeation process though the SCSc membranes is predominated by the oxygen surface exchange kinetics with the activation energy of 95.0 kJ mol^{-1}.

Acknowledgements

The authors gratefully acknowledge the research funding provided by the National High Technology Research and Development Program of China (No. 2006AA03Z464), the National Natural Science Foundation of China (No. 20676073) and Natural Science Foundation of Shandong Prov. (Y2007F18, Y2008B07). Shaomin Liu acknowledges the ARC fellowship provided by the Australian Research Council.

References

1. Armstrong, P. A., Foster, E. P., Horazak, D. A., Morehead, H. T. and Stein, V. E., Ceramic and coal: ITM oxygen for IGCC. In *Proceedings of the 22nd International Pittsburgh Coal Conference*, 2005.
2. Ullmann, H. and Trofimenko, N., Composition, structure and transport properties of perovskite-type oxides. *Solid State Ionics*, 1999, **119**, 1–8.
3. Xu, S. J. and Thomson, W. J., Oxygen permeation rates through ion-conducting perovskite membranes. *Chem. Eng. Sci.*, 1999, **54**, 3839–3850.
4. Balachandran, U., Ma, B., Maiya, P. S., Mieville, R. L., Dusek, J. T., Picciolo, J. J., Guan, J., Dorris, S. E. and Liu, M., Development of mixed-conducting oxides for gas separation. *Solid State Ionics*, 1998, **108**, 363–370.
5. Kharton, V. V., Yaremchenko, A. A., Kovalevsky, A. V., Viskup, A. P., Naumovich, E. N. and Kerko, P. F., Perovskite-type oxides for high-temperature oxygen separation membranes. *J. Membr. Sci.*, 1999, **163**, 307–317.
6. Vente, J. F., Haije, W. G. and Rak, Z. S., Performance of functional perovskite membranes for oxygen production. *J. Membr. Sci.*, 2006, **276**, 178–184.
7. Shaula, A. L., Yaremchenko, A. A., Kharton, V. V., Logvinovich, D. I., Naumovich, E. N., Kovalevsky, A. V., Frade, J. R. and Marques, F. M. B., Oxygen permeability of $LaGaO_3$-based ceramic membranes. *J. Membr. Sci.*, 2003, **221**, 69–77.
8. Kharton, V. V., Viskup, A. P., Marozau, I. P. and Naumovich, E. N., Oxygen permeability of perovskite-type $Sr_{0.7}Ce_{0.3}MnO_{3-\delta}$. *Mater. Lett.*, 2003, **57**, 3017–3021.
9. Shao, Z., Xiong, G., Dong, H., Yang, W. and Lin, L., Synthesis, oxygen permeation study and membrane performance of a $Ba_{0.5}Sr_{0.5}Co_{0.8}Fe_{0.2}O_{3-\delta}$ oxygen-permeable dense ceramic reactor for partial oxidation of methane to syngas. *Sep. Purif. Technol.*, 2001, **25**, 97–116.
10. Fan, C., Zuo, Y., Li, J., Lu, J., Chen, C. and Bae, D., Highly permeable $La_{0.2}Ba_{0.8}Co_{0.8}Fe_{0.2-x}Zr_xO_{3-\delta}$ membranes for oxygen separation. *Sep. Purif. Technol.*, 2007, **55**, 35–39.
11. Ito, W., Nagai, T. and Sakon, T., Oxygen separation from compressed air using a mixed conducting perovskite-type oxide membrane. *Solid State Ionics*, 2007, **178**, 809–816.
12. Kovalevsky, A. V., Kharton, V. V., Tikhonovich, V. N., Naumovich, E. N., Tonoyan, A. A., Reut, O. P. and Boginsky, L. S., Oxygen permeation through $Sr(Ln)CoO_{3-\delta}$ (Ln = La, Nd, Sm, Gd) ceramic membranes. *Mater. Sci. Eng. B.*, 1998, **52**, 105–116.
13. Cheng, Y., Zhao, H., Teng, D., Li, F., Lu, X. and Ding, W., Investigation of Ba fully occupied A-site $BaCo_{0.7}Fe_{0.3-x}Nb_xO_{3-\delta}$ perovskite stabilized by low concentration of Nb for oxygen permeation membrane. *J. Membr. Sci.*, 2008, **322**, 484–490.
14. Li, S., Cong, Y., Fang, L., Yang, W., Lin, L., Meng, J. and Ren, Y., Oxygen permeating properties of the mixed conducting membranes without cobalt. *Mater. Res. Bull.*, 1998, **33**, 183–188.
15. Doorn, R. H. E., Bouwmeester, H. J. M. and Burggraaf, A. J., Kinetic decomposition of $La_{0.3}Sr_{0.7}CoO_{3-\delta}$ perovskite membranes during oxygen permeation. *Solid State Ionics*, 1998, **111**, 263–272.
16. Tong, J., Yang, W., Zhu, B. and Cai, R., Investigation of ideal zirconium-doped perovskite-type ceramic membrane materials for oxygen separation. *J. Membr. Sci.*, 2002, **203**, 175–189.
17. Diethelm, S., van Herle, J., Middleton, P. H. and Favrat, D., Oxygen permeation and stability of $La_{0.4}Ca_{0.6}Fe_{1-x}Co_xO_{3-\delta}$ ($x = 0, 0.25, 0.5$) membranes. *J. Power Sources*, 2003, **118**, 270–275.
18. Kharton, V. V., Tsipis, E. V., Yaremchenko, A. A., Marozau, I. P., Viskup, A. P., Frade, J. R. and Naumovich, E. N., Oxygen permeability, electronic conductivity and stability of $La_{0.3}Sr_{0.7}CoO_3$-based perovskites. *Mater. Sci. Eng. B*, 2006, **134**, 80–88.
19. Lu, H., Tong, J., Deng, Z., Cong, Y. and Yang, W., Crystal structure, oxygen permeability and stability of $Ba_{0.5}Sr_{0.5}Co_{0.8}Fe_{0.1}M_{0.1}O_{3-\delta}$(M = Fe, Cr, Mn, Zr) oxygen-permeable membranes. *Mater. Res. Bull.*, 2006, **41**, 683–689.
20. Nagai, T., Ito, W. and Sakon, T., Relationship between cation substitution and stability of perovskite structure in $SrCoO_{3-\delta}$-based mixed conductors. *Solid State Ionics*, 2007, **177**, 3433–3444.
21. Zeng, P., Ran, R., Chen, Z., Gu, H., Shao, Z. and Liu, S., Novel mixed conducting $SrSc_{0.05}Co_{0.95}O_{3-\delta}$ ceramic membrane for oxygen separation. *AIChE J.*, 2007, **53**, 3116–3124.
22. Luyten, J., Buekenhoudt, A., Adriansens, W., Cooymans, J., Weyten, H., Servaes, F. and Leysen, R., Preparation of $LaSrCoFeO_{3-x}$ membranes. *Solid State Ionics*, 2000, **135**, 637–643.
23. Tan, X., Liu, Y. and Li, K., Preparation of LSCF ceramic hollow fibre membranes for oxygen production by a phase-inversion/sintering technique. *Ind. Eng. Chem. Res.*, 2005, **44**, 61–66.
24. Schiestel, T., Kilgus, M., Peter, S., Caspary, K. J., Wang, H. and Caro, J., Hollow fibre perovskite membranes for oxygen separation. *J. Membr. Sci.*, 2005, **258**, 1–4.
25. Tablet, C., Grubert, G., Wang, H., Schiestel, T., Schroeder, M., Langanke, B. and Caro, J., Oxygen permeation study of perovskite hollow fibre membranes. *Catal. Today*, 2005, **104**, 126–130.
26. Liu, S. and Gavalas, G. R., Oxygen selective ceramic hollow fibre membranes. *J. Membr. Sci.*, 2005, **246**, 103–108.
27. Li, K., Tan, X. and Liu, Y., Single-step fabrication of ceramic hollow fibres for oxygen permeation. *J. Membr. Sci.*, 2006, **272**, 1–5.
28. Tan, X., Liu, Y. and Li, K., Mixed conducting ceramic hollow fibre membranes for air separation. *AIChE J.*, 2005, **51**, 1991–2000.
29. Tan, X. and Li, K., Modeling of air separation in a $La_{0.6}Sr_{0.4}Co_{0.2}Fe_{0.8}O_{3-\delta}$ hollow fibre membrane module. *AIChE J.*, 2002, **48**, 1469–1477.
30. Liu, S., Tan, X., Shao, Z. and Costa, D. J. C., $Ba_{0.5}Sr_{0.5}Co_{0.8}Fe_{0.2}O_{3-\delta}$ ceramic hollow fibre membranes for air separation. *AIChE J.*, 2006, **52**(10), 3452–3461.
31. Wang, Z., Yang, N., Meng, B. and Tan, X., Preparation and oxygen permeation properties of highly asymmetric $La_{0.6}Sr_{0.4}Co_{0.2}Fe_{0.8}O_{3-\alpha}$ (LSCF) perovskite hollow fibre membranes. *Ind. Eng. Chem. Res.*, 2009, **48**(1), 510–516.